LA-UR-12-23870
Approved for public release; distribution is unlimited.

Title: Proton radiography: its uses and resolution scaling

Author(s):
Mariam, Fesseha G.
Merrill, Frank E.
Espinoza, Camilo J.
Heidemann, Joel A.
Hollander, Brian J.
Kwiatkowski, Kris K.
Lopez, Julian D.
Lopez, Robert P.
Marr-Lyon, Mark
McNeil, Wendy V.
Morley, Deborah J.
Morris, Christopher
Murray, Matthew M.
Nedrow, Paul
Perry, John O.
Saunders, Alexander
Tainter, Amy M.
Trouw, Frans R.
Tupa, Dale

Intended for: Journal of Applied Remote Sensing

Proton radiography: its uses and resolution scaling

F.G. Mariam, F.E. Merrill, C.J. Espinoza, J.A. Heidemann, B.J. Hollander, K.K. Kwiatkowski, J.D. Lopez, R.P. Lopez, M. Marr-Lyon, W.V. McNeil, D.J. Morley, C. Morris, M.M. Murray, P. Nedrow, J.O. Perry, A. Saunders, A.M. Tainter, F.R. Trouw, D. Tupa

(Los Alamos National laboratory, Los Alamos, NM 87544)

ABSTRACT

Modern proton radiography (pRad), which was invented at the Los Alamos National Laboratory (LANL), is especially well suited for investigation of dense materials. When compared to x-radiography, the mean free path of protons is much longer resulting in near-optimum radiographic transmission. The proton radiography facility at LANL which utilizes the 800 MeV proton beam at the Los Alamos Neutron Sciences Center (LANSCE), is a user facility mainly serving the weapons community. The temporal structure of the beam coupled with high quantum efficiency multi-frame cameras has enabled the acquisition of up to 41 radiographic frames over the duration of dynamic processes typically lasting a few tens of microseconds. Sample results from the pRad facility at LANL are presented. The position resolution of proton radiography can be improved both by using higher energy proton beams and by using magnifying lenses. We present theoretical studies for both improvements.

Keywords: proton radiography, flash radiography, tomography

1. INTRODUCTION: OUTLINE OF MODERN PROTON RADIGRAPHY

As energetic protons pass through an object, there are three basic processes that are of relevance to proton radiography: 1) Elastic and inelastic nuclear scattering that result in the attenuation of the transmitted flux through absorption or large angle scattering, 2) Ionization energy loss and energy straggling through interactions with electrons in the medium, 3) Multiple Coulomb scattering due to Coulomb interactions with the nuclei of the medium resulting in small deflections of the proton trajectories.

Early attempts at proton radiography used marginal energy ranging(Koehler) where, in the last mm or so of their range, the large energy loss of the protons was utilized to produce high contrast images of thin objects. However, multiple Coulomb scattering became a major source of blur, especially if the distance from the object to the detector (converter) was more than a few cm. A number of researchers continued to experiment with proton radiography, resulting in incremental improvements. But the blur due to multiple Coulomb scattering remained a serious problem until Morris suggested the concept of lens focused high energy proton radiography.

Modern proton radiography utilizes magnetic quadrupole imaging lenses arranged in the Russian quadruplet configuration(C. Thomas Motterhead). We will describe components of this system in so far as it helps elucidate our presentation. An illustration of a magnetic lens with a magnification of -1 is shown in figure 1.The imaging lens is made of four electromagnets. It consists of two identical quad doublets and is reflection-symmetric about the longitudinal mid-plane. For a monochromatic beam, all protons originating at a point $(x_o\,, x'_0\,, y_o\,, y'_0)$ at the "object plane" are imaged onto a point $(x_i\,, x'_i\,, y_i\,, y'_i)$ at the image plane:

$$x_i = R_{11}x_o + R_{12}x'_o \qquad y_i = R_{33}y_o + R_{34}y'_o \tag{1.1}$$

where the R_{ij} are elements of the first order beam transfer matrix of the imaging lens. *x, y* are the position, and *x', y'* are the angle coordinates in the transverse plane. The condition for image formation is that $R_{12} = R_{34} = 0$. We note that, in figure 1, all rays originating at a given point at the object plane are focused at the image plane. Since the lens can be set to focus at only one proton energy, this can only be true for monochromatic rays. For geometrically complex objects, protons passing through thicker portions of the object have, on the average, lower energy than those passing through thinner parts. Even for flat objects, energy straggling introduces a spread in the energy of the emerging protons. This gives rise to chromatic blur. The resulting blur can be represented by a second order modification to eqn. 1.1 and is given by:

$$\delta x_i = [T_{116}x_o + T_{126}(x'_o + \theta)]\frac{\delta p}{p}, \qquad \delta y_i = [T_{336}y_o + T_{346}(y'_o + \theta)]\frac{\delta p}{p} \qquad (1.2)$$

where, θ is the angular deflection due to multiple Coulomb scattering at the object. The second order coefficients, $T_{116} = \frac{\partial R_{11}}{\partial p}p$, $T_{126} = \frac{\partial R_{12}}{\partial p}p$, etc are chromatic terms intrinsic to the imaging lens and $\frac{\delta p}{p}$ is the fractional deviation in momentum with respect to the lens focus setting, *p*. Mottershead and Zumbro(C. Thomas Motterhead), showed that the beam ellipse in $(x_o\ , x'_0)$ space at the object plane can be prepared such that the correlation $\frac{x_o}{x'_0} = -\frac{T_{126}}{T_{116}}$ and similarly in the $(y_o\ , y'_0)$ space . We are then left with a reduced chromatic blur given by:

$$\delta x = T_{126}\theta\frac{\delta p}{p}, \qquad \delta y = T_{346}\theta\frac{\delta p}{p} \qquad (1.3)$$

with the position-dependent terms T_{116}, T_{336} no longer contributing to the blur.

This scheme of "matching" the incoming beam correlation to the chromatic properties of the magnetic imaging lens also has the consequence that, at the Fourier plane, protons are sorted into radial positions in proportion to their angular deflection due to multiple Coulomb scattering. This is indicated by the ray trace diagram in figure 1. Since the blur is proportional to this angle, a restriction at the Fourier plane, that filters out protons scattered to large angles, results in better resolution. Other means of mitigating blur will be discussed at length in section 3.

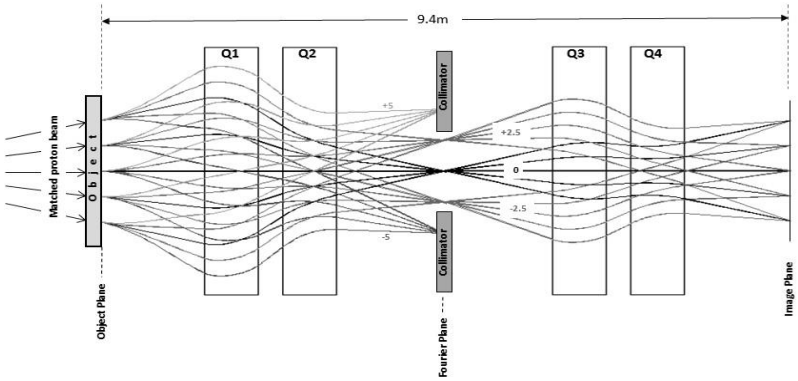

Figure 1. A COSY (beam-optic code) rendition of the x1 magnetic imaging lens made up of quadrupole electromagnets Q1, Q2, Q3 and Q4. The incoming proton beam is arranged as indicated, where the direction of the protons is correlated to their positions with respect to the optical axis of the quadrupoles. This is the matching condition discussed in the text. For a beam arranged in such manner, the protons are sorted into radial positions at the Fourier Plane; the radial position depends *only* on the angular deflection suffered by the proton due to Coulomb scattering at the "object". The sorted ray bundles near Fourier plane are labeled by the angular deflection in mradians. Placing an aperture restriction (collimator) at the Fourier plane, removes protons that have scattered through large angles. Use of small collimators leads to enhanced resolution.

The proton transmission *T* through an object is well represented by a product of the nuclear attenuation and the transmission through the collimator at the Fourier plane

$$T = e^{-\frac{\rho X}{\lambda}}\left(1 - e^{-\frac{\theta_c^2}{2\theta_0^2}}\right) \qquad (1.4)$$

where $\theta_0 = \frac{14.1}{\beta p}\sqrt{\frac{\rho X}{X_0}}$ is the rms scattering angle; β and p [MeV/c] are the relativistic velocity and momentum of the proton beam, respectively; θ_c is the angular size of the collimator; λ, X_0 and ρ are the nuclear collision length, the radiation length and the density of the object, and X is the thickness of the object in the beam direction. Given a transmission radiograph, a slightly more complicated version of equation 1.4 that includes background, can be applied to extract the areal density ρX of the object. While the use of a small collimator enhances the resolution it also limits the

transmission. The optimum collimator size for a given experiment can be chosen using a figure of merit based on the product of the resolution and the transmission given by equation 1.4. (C.L. Morris).

2. PROTON RADIOGRAPHY AT LANL

There are three magnetic imaging lenses available to experimenters at the LANSCE pRad facility; an identity lens (-I lens) with unit magnification(C. Thomas Motterhead), a magnifier lens (x3) with a magnification of 2.7(F.E. Merrill) and another magnifying lens (x7) with a magnification of 7 (MOTTERSHEAD). The setup of the –I and x3 lenses, with illustrative ray diagrams, are shown in figures 2a and 2b and some of the pertinent properties of the three systems are given in table 1. The object is placed at the "object location" and, except for some air gaps at the image locations indicated in figure 2, the beam line (including the object) is under vacuum. While it is possible to build collimators tailored for any experiment, the common practice is to choose one from a suite of available collimators that best approximates the optimum for a given experiment.

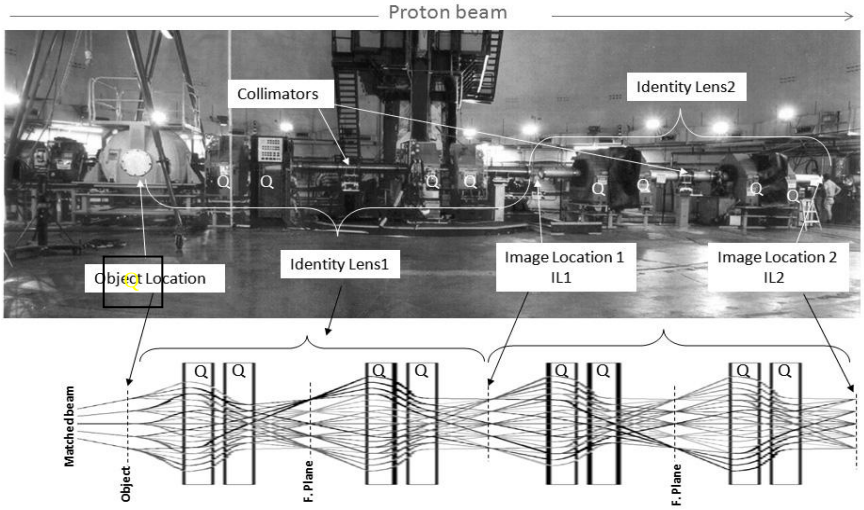

Figure 2a: Layout of the pRad facility at LANL showing the two identity lenses in series. For dynamic experiments, the object is placed at the center of the confinement vessel ("Object Location"). Two identity lenses are shown. The first lens forms an image at IL1 and the second at IL2. The converter at IL1 is protected from blast by an aluminum window. The collimators are aperture restrictions at the Fourier plane of each lens.

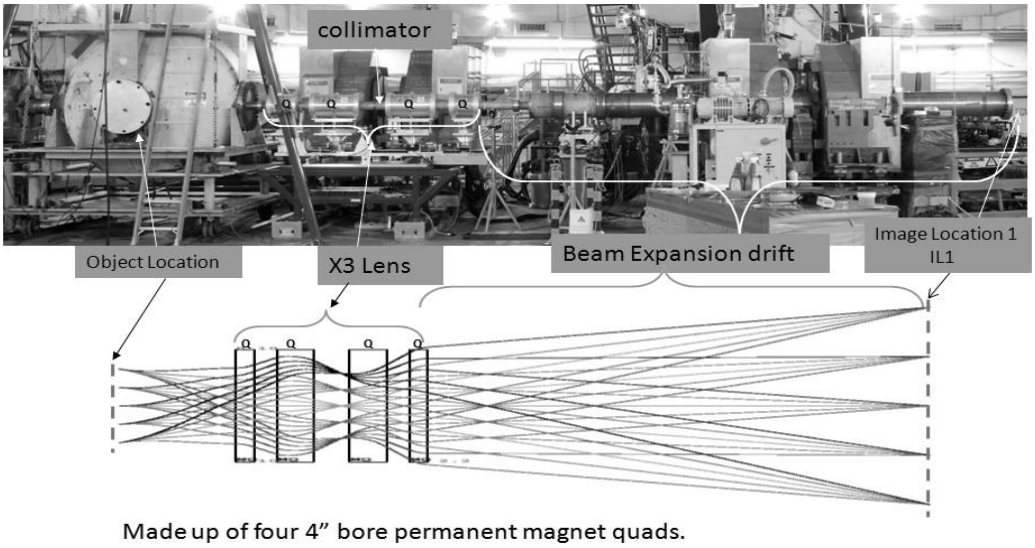

Figure 2b: The x3 magnifier is made up of four permanent magnet quadrupols. They replace the first two quadrupoles (shown in the background) of the identity lens. The active imaging quadrupoles between the object and image locations are labeled "Q".

Having passed through the object, the imaging magnetic lens focuses the transmitted protons on an LSO (lutetium Oxyorthosilicate) converter at the image plane. The resulting light out of the converter is guided onto a set of cameras which are focused at the image plane. A schematic description of the optical train is shown in figure 3(a).

Table 1. Radiographic parameters of the three imaging lenses at the LANL pRad facility. T126 and T346 are the chromatic lengths in the x and y planes, respectively. The "total resolution is" the overall system resolution due to the magnetic imaging lens and the blur due to the detector and the camera optics. It is the RMS width from a Gaussian erf function fit to a radiograph of the edge of a 3mm thick tungsten plate.

LENS SYSTEM (Bore)	Magnification	FOV (mm)	T126 (Normalized) (m)	T346 (Normalized) (m)	Total Resolution (μm)
LENS2 (12")	-1	120	7.9	7.9	180
X3 Magnifier (4")	-2.7	40	4.1	3.3	65
X7 Magnifier (1")	-7	17	1.2	1.9	~30

2.1 Flash Radiography

The pRad facility at LANSCE is mainly used in flash radiography mode in the study of energetic materials driven by explosives. Typical dynamic processes last a few tens of microseconds. The LANSCE LINAC delivers 625μs long proton pulses at 60Hz or, for flash radiography, in single pulse mode and on demand. A programmable beam chopper in the front-end section of the LANSCE linac is used to set up almost any desired beam micro-pulse pattern. Almost any number (more than 100) of beam micro pulses can be spread arbitrarily across the 625μs long beam macro pulse, with a minimum separation of 200ns. For most flash radiography applications each micro pulse has between 3 to $5x10^9$ protons. As the dynamic event progresses, each beam micro pulse illuminates the object and the image formed at the LSO is recorded by a synchronously gated camera. The temporal relationship between the explosive drivers, the beam structure and the camera gates is illustrated schematically in figure 3(b). The LANSCE pRad facility can provide a multi-frame capability of up to 41 frames per dynamic event – limited only by the number of detectors(Kris Kwiatokowski). This is a great advantage in studying the time evolution of dynamic processes. Some representative pRad flash-radiographic results are shown in figures 4 to 6.

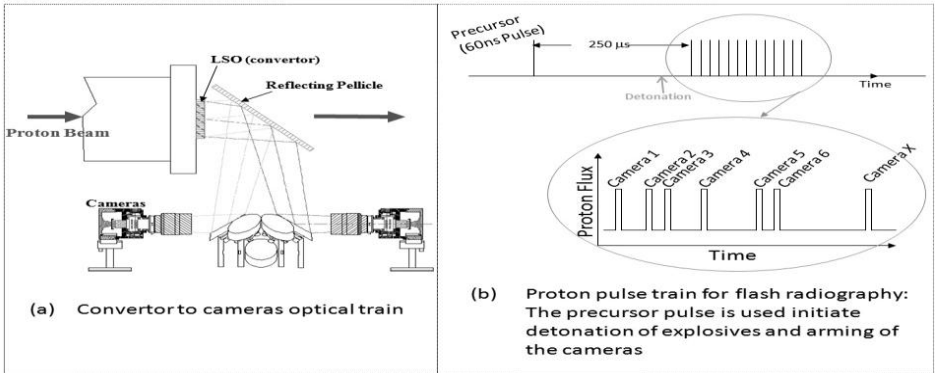

Figure 3. (a) The camera arrangement at the two image locations (IL1 and IL2). There are seven cameras at IL1; one is a single-frame camera and the rest are 3-frame cameras(Kris Kwiatokowski) providing a total of 19 frames. Additional 13 frames are acquired at IL2, giving a total of 41 frames per dynamic event. (b) The precursor proton pulse which comes 250μs ahead of the first camera pulse, is used to arm the cameras and, with proper delays, to initiate detonation of explosives that drive dynamic experiments.

2.2 Other Uses

There is steadily increasing use of the facility for the study of static and quasi-static processes. Again, this is due the versatility of the LANSCE beam and the multi frame camera system. The frame rate for such experiments is typically 0.5 to 10Hz and radiographic data is acquired by the multi frame cameras which are set to run synchronously in movie mode. Some examples (out of numerous experiments), are given below:

1. An important preliminary experiment on surrogate materials has shown that, the x3 magnetic lens can be used to produce tomographic images of nuclear fuel rods which showed that sub-millimeter defects can be detected with a resolution of about 80 microns (see figure 7). In addition to that shown in figure 7, an extensive set of data were collected on other surrogate fuel rods with known defects and known density variations. Analysis of the data confirmed that sub-millimeter defects can be mapped accurately and that density determinations can be made with about 2% uncertainty. (C. L. Morris)
2. Exothermic reaction of formation of refractory materials such as tantalum siliscide, titanium carbide, etc. have been radiographed to determine the reaction rates, the directionality of the burn front and the dynamic density changes associated with such chemical reactions. Effects of reactant concentrations on the burn velocity and directionality have been observed. Preliminary radiographs are shown in figure 8.
3. In-situ observation of the dynamic behavior of metal alloys under melting and solidification phase transformations were conducted, for the first time ever, using the x3 magnetic imaging lens at the LANL pRad facility. Radiographs of such process in Al-In alloy are shown in figure 9.

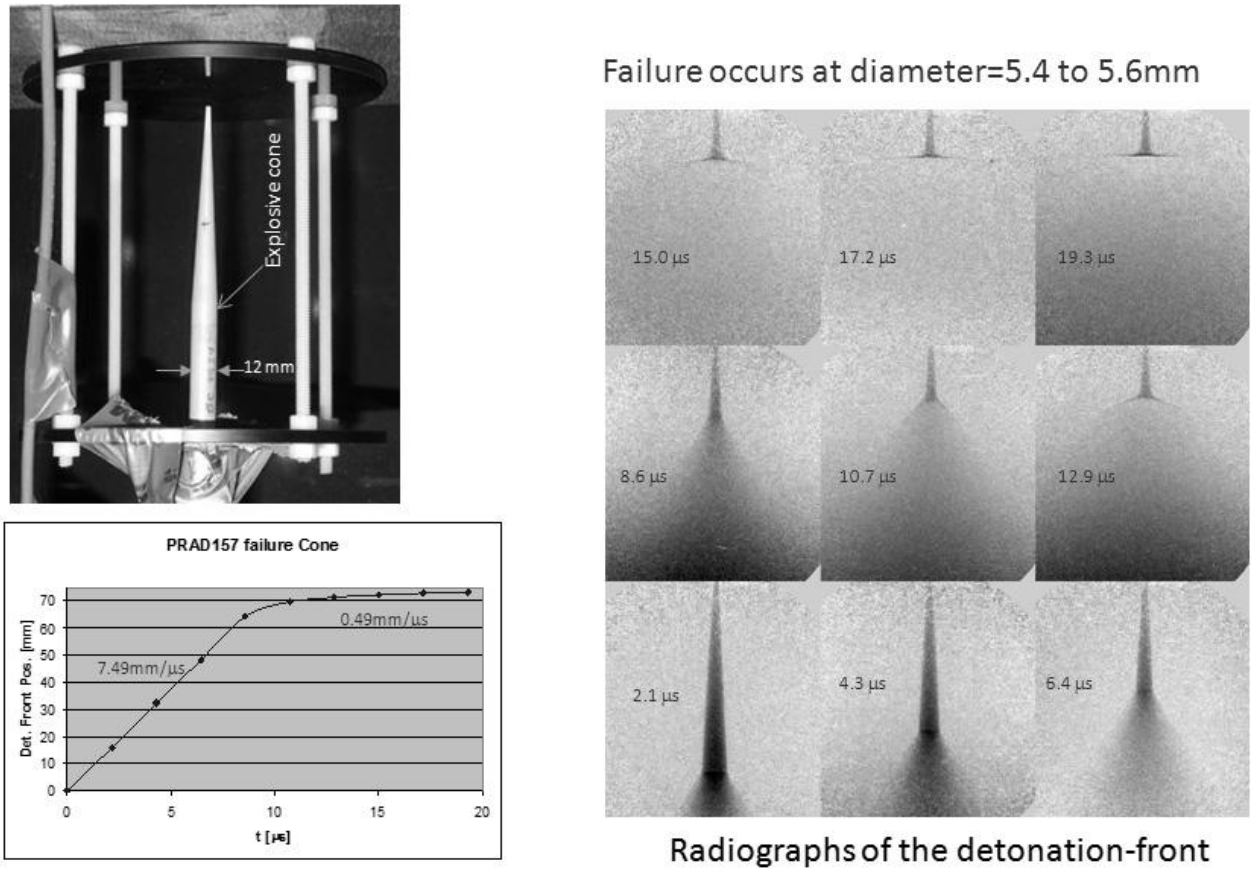

Figure 4: A conical shaped charge is used to study the propagation characteristics of the detonation front through the varying charge diameter. Detonation is initiated at the base of the cone and propagates toward the cone apex until it reaches a critical diameter below which a steady detonation wave is not able to support itself. (Eric N Ferm). Radiographs like these have been used to study the details of the transition zone near failure of detonation.

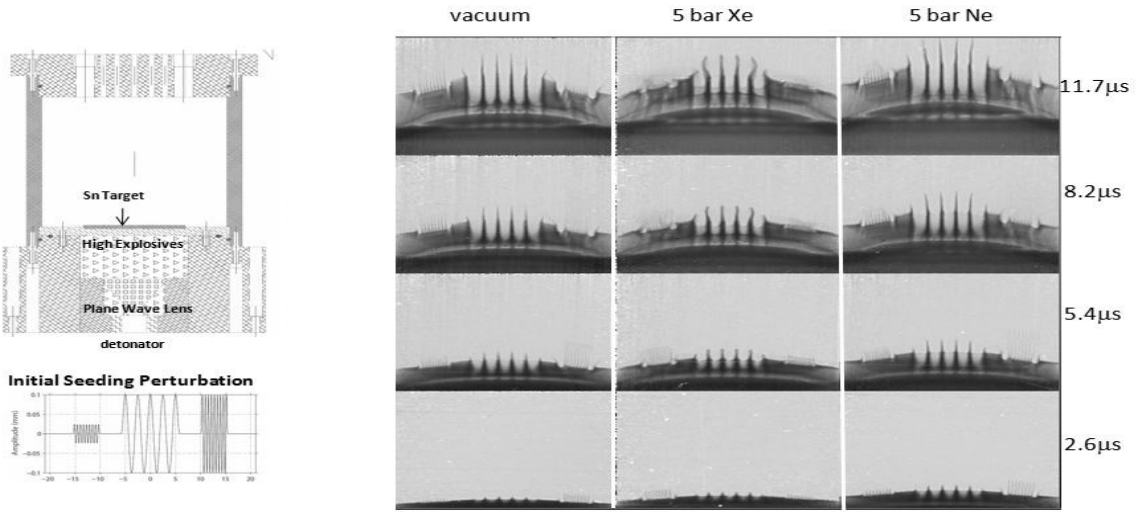

Figure 5: Richtmyer-Meshkov instability studies in tin utilizing the x3 magnifier at the LANSCE pRad. A thin coupon of tin, with three groups of perturbations etched onto the surface, is driven by a plane wave lens (shown on the left). Radiographs of the time-evolution of the instability in vacuum, in Xe and in Ne at 5 bars are shown on the left. Such measurements on the growth of the instability have provided critical data for the development of eject models. (D. O. W.T. Buttler)(e. a. W.T. Buttler)

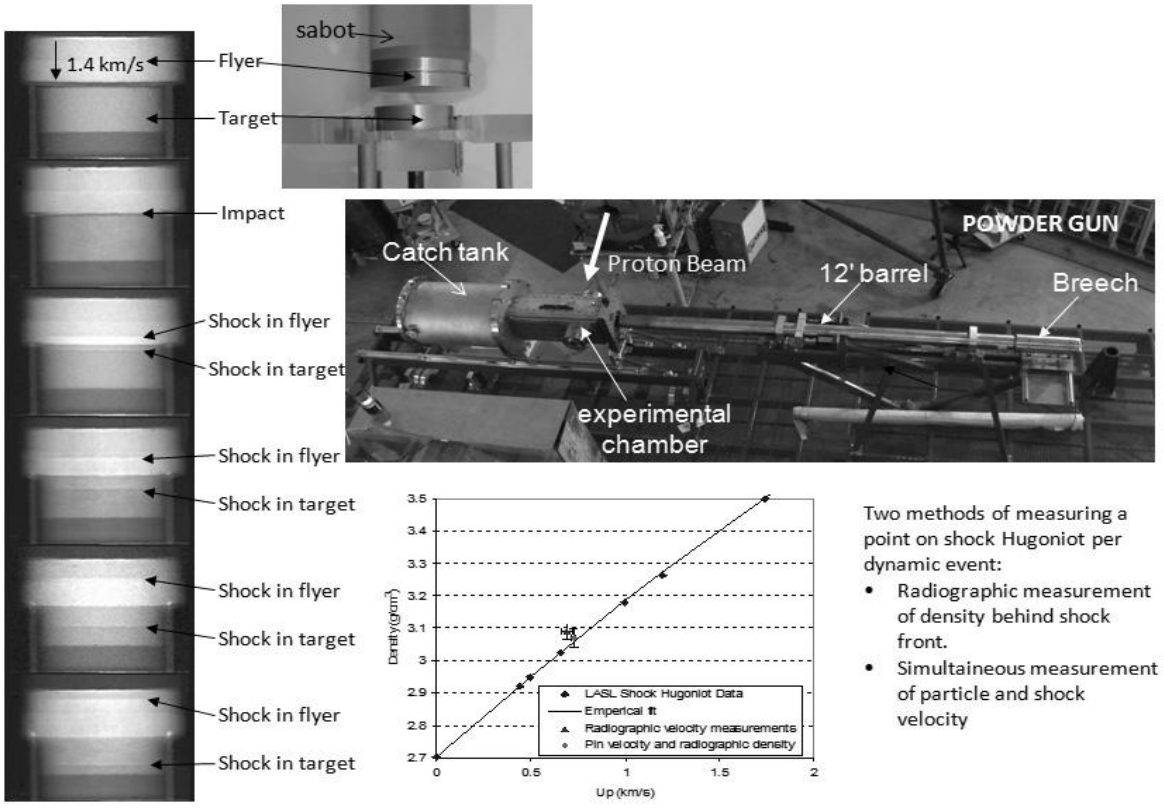

Figure 6: An aluminum flyer (sabot) launched by a powder gun impacts an aluminum disc. The shock waves generated by the impact travel into the target and into the flyer. The densities of the shocked and un-shocked regions can be inferred from the radiographs and when combined with the particle velocities (also inferred from the radiographs) predict a point in the shock Hugoniot of Aluminum [(P.A. Rigg)]. Similar experiments have been conducted on copper and iron. In the case of iron solid-solid phase transitions have been observed.

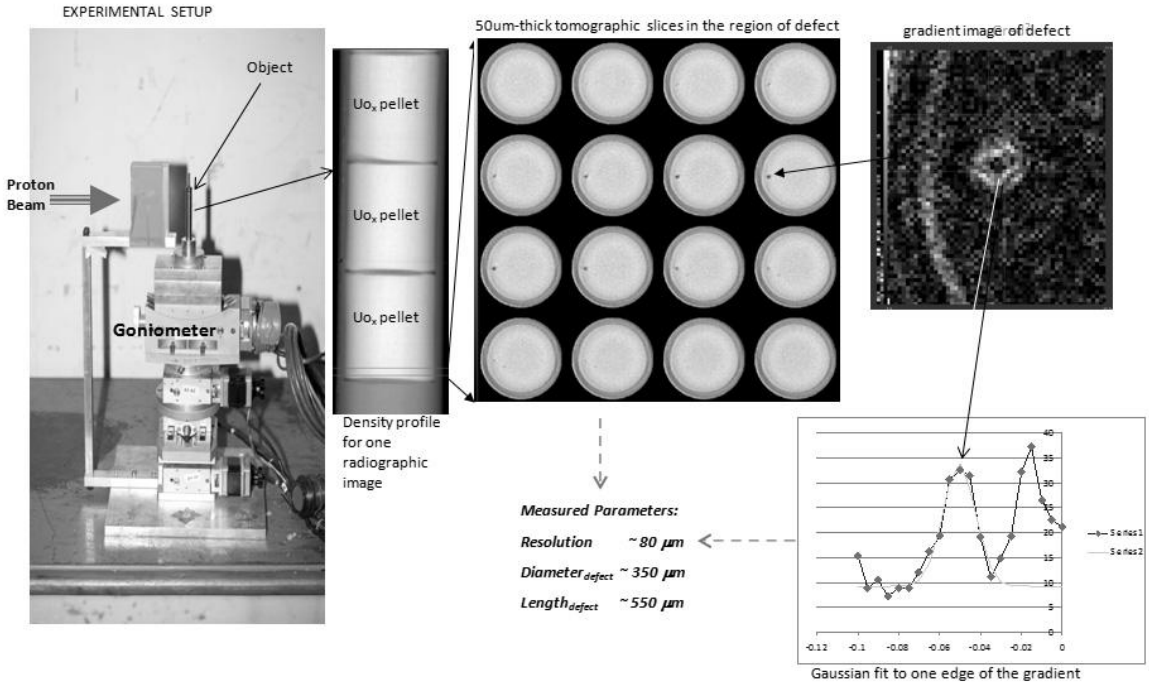

Figure 7. Tomography of surrogate nuclear fuel pellets. The 1-cm diameter pellets were housed inside a zircaloy tubing and mounted on a goniometer. Tomographic reconstruction was performed from 180 radiographic images taken in 1^{o} steps. The 50μm-thick slices from the tomographic reconstruction are in the vicinity of a manufacturing defect in one of the pellets.

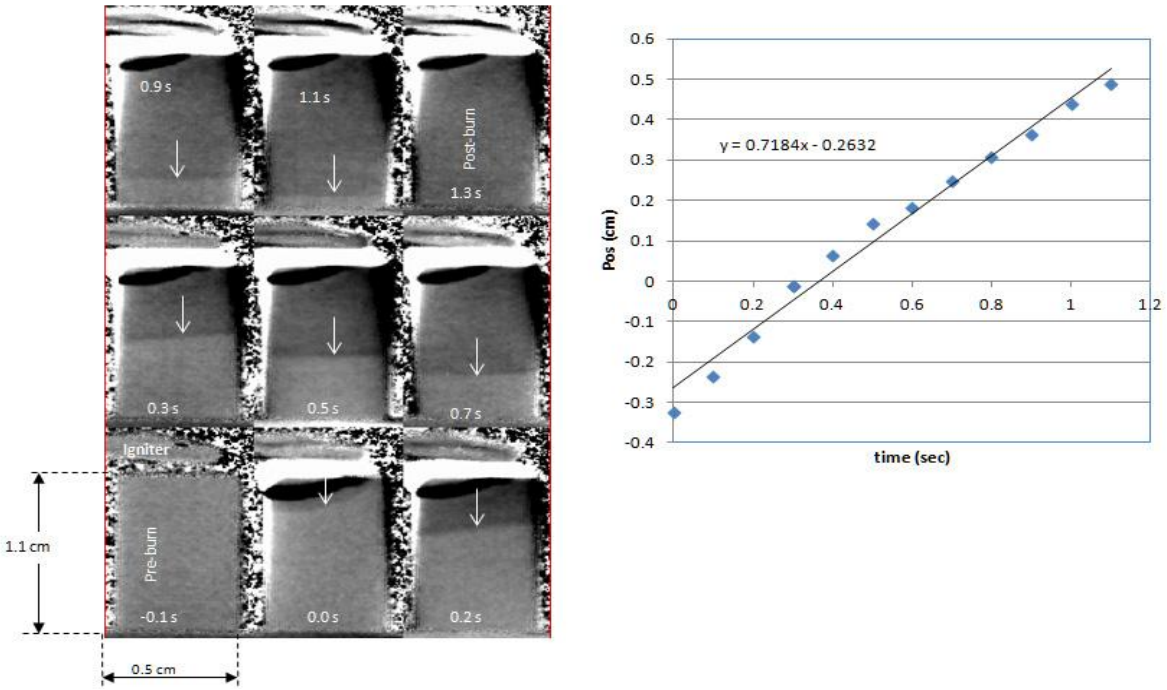

Figure 8. The propagation of the burn front in the exothermic formation of tantalum silicide (Ta_5Si_3) in a pressed powder mixture of tantalum and silicon are indicated by the arrows. The time-stamped frames shown are the ratio of the post to pre-burn images. The reaction is initiated by a heating filament (igniter) at the top. The radiographic images were taken in movie mode at 10Hz. The average burn front velocity is about 0.7cm/s and the density change due to the reaction is -5% to 6%. Detailed analysis is in progress.

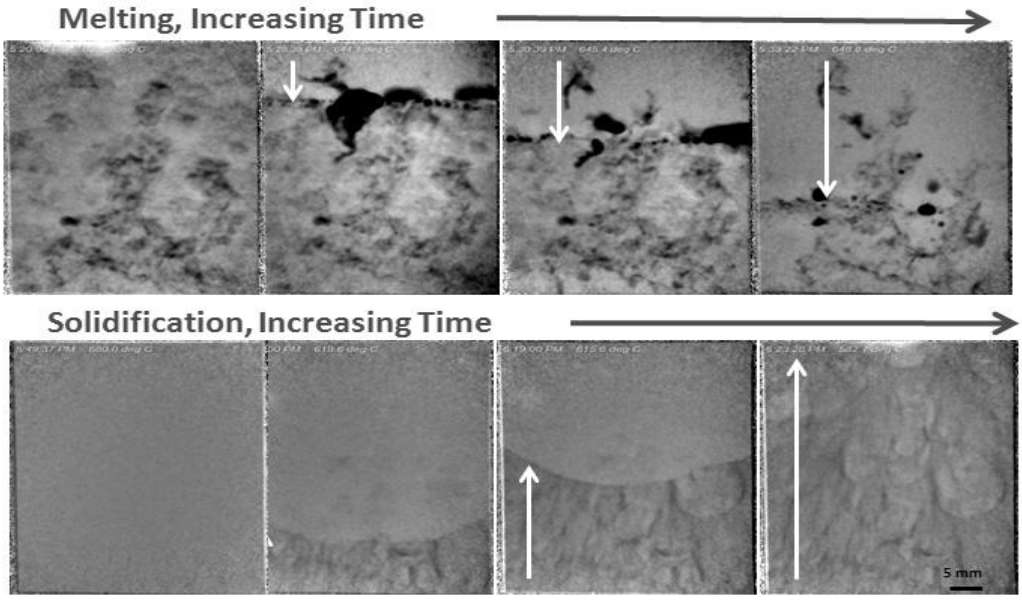

Figure 9. In-situ monitoring of In-Al alloy melt fluid flow and solidification using pRad. The darker regions in the solid phase and solid-liquid interface are identified as indium-rich regions. These are the first in-situ images ever of alloy melting and solidification processes.(A.J. Clarke)

3 RESOLUTION SCALING FOR PROTON RADIOGRAPHY

We have explored several avenues to improve the performance of proton radiography. At the LANSCE beam energy of 800MeV, magnifier lenses provide improved resolution with a proportionately diminished field of view (FOV).The x3 magnifier in use at the LANSCE pRad facility has been described elsewhere.(F.E. Merrill). Another lens, with an approximate magnification of x7 had also been commissioned at the LANSCE pRad facility (MOTTERSHEAD). The radiographic parameters for these lenses are given in table 1.

We discuss the scaling methods toward higher resolution, taking into account our experience with imaging at 7 and 20GeV at Brookhaven National Laboratory and utilizing beam optic analysis tools. There are three main processes that contribute to limit the resolution of a proton radiography system: a) object scattering which is introduced as the protons are scattered while traversing the object, b) chromatic aberrations, which, as discussed previously, are intrinsic to the magnetic lens, and c) detector blur which is introduced as the protons interact with the radiation to light convertor and by the optical train including the cameras.

3.1 Object Scatter Blur

Multiple Coulomb scattering of protons as they traverse the object results in small deflections of the proton trajectories. After leaving the object the proton is focused by the magnetic lens to form an image and this deflection results in blur at the image location. This process is shown pictorially in figure 10. The incident proton passes through the object to the point of interest, typically a region in the center of the object. Scattering upstream of the point of interest does not resulting in significant contribution to the blur function. Scattering downstream of the object, however, results in a small position offset and a small angular deflection, which results in a small error in the position of the proton at the image location. Because multiple-Coulomb scattering results in nearly a Gaussian distribution of scatter angles, the resulting point spread function is very close to a Gaussian distribution. The rms width of the resulting blur function can be represented by,

$$\sigma_0 = \frac{1}{\sqrt{3}}\theta l = \frac{14.1}{\sqrt{3}}\frac{1}{p\beta}\sqrt{\frac{\rho l^3}{X_o}} \propto \frac{l^{3/2}}{p} \qquad (3.1)$$

Where the variables in the above equation are: θ is the RMS angular deflection of the proton, p is the proton momentum in MeV/c, $\beta = v/c$ is the relativistic velocity; ρ, X_o are the density and the radiation length of the object material,

respectively. Thus, this blur source scales inversely with the incident proton momentum and the resolution improves as the incident proton momentum increases.

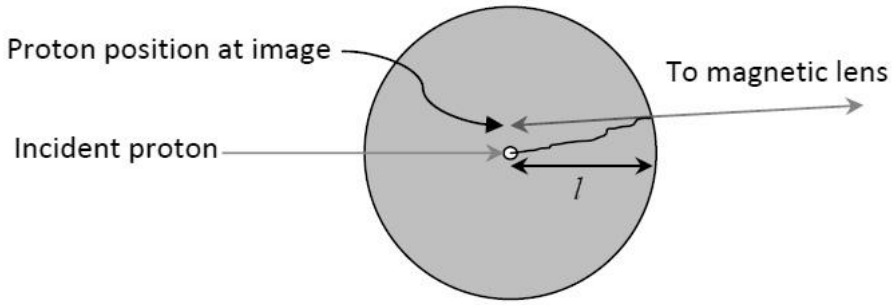

Figure 10: Object scatter blur results from small angle scattering within the object, downstream of the point of interest. The small angular deflection results in a small position error at the image location as the proton is focused by the magnetic lens system.

3.2 Chromatic Aberrations

As discussed earlier, chromatic aberrations, which also contribute to image blur, are a result of off-momentum protons being focused differently by the magnetic imaging lens system. The relationship of the RMS blur (σ_c), which is typically a Gaussian point spread function, to the scattering angle, θ, the fractional momentum offset ($\delta p/p$) and the chromatic length of the lens system $l_c = T_{126} \approx T_{346}$ is given by,

$$\sigma_c = l_c\theta\frac{\delta p}{p} = c\sqrt{p}\frac{\delta p}{p^2}\frac{14.1}{\beta}\sqrt{\frac{\rho l}{X_o}} \propto \sqrt{\frac{l}{p^3}}$$ (Eric N Ferm)

(Koehler)(3.3)

Simple models and calculations using beam-optic codes both show that for a conventional (non-superconducting) non-magnifying magnetic lens system, with pole-tip fields of ~1T and a field of view of ~100mm, the chromatic length of the lens system grows as the square root of the proton momentum. This is shown in figure 11. Therefore, the chromatic resolution for relativistic protons scales inversely with momentum to the three-halves power.

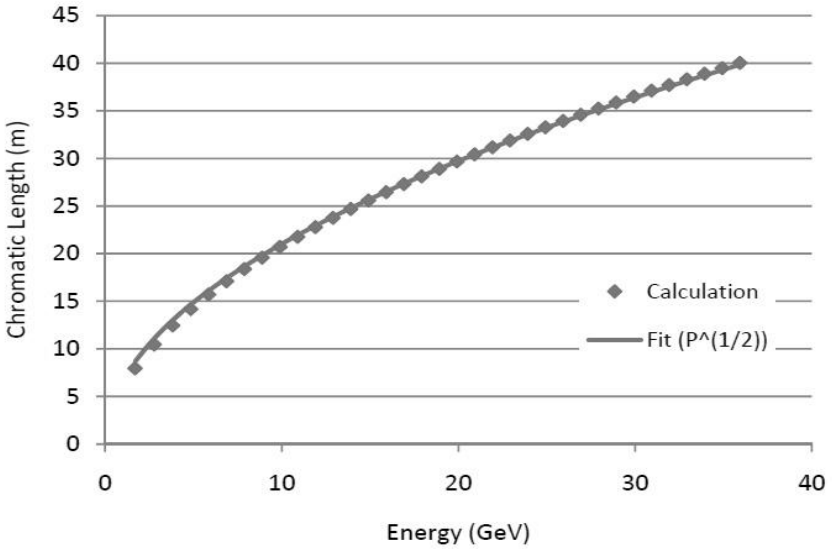

Figure 11: The chromatic length of a conventional imaging lens system with ~1 T pole tip field was calculated for systems with ~100 mm field of view for various proton energies. The chromatic length increases as the square-root of the proton momentum.

3.3 Detector Blur

The contribution from the detector system (proton-light converter and imaging cameras) to the radiographic resolution is independent of momentum and object thickness. Present technologies deployed for 800MeV proton radiography have ~100 micron resolution in the image plane. This meets the requirements of the present radiographic capability. However, this is not a fundamental limit and detector development may be needed to push the resolution contribution down to match improved radiographic resolution.

3.4 Scaling of measured 800 MeV Proton Radiography Resolution

The thin object resolution of 800 MeV proton radiography with a –I lens, including radiographic and detector contributions, has been measured to be 180 microns. The radiographic resolution alone is estimated to be ~100 microns. The radiographic resolution can then be scaled according to the scaling laws described above. Figures 12(a) and 12(b) show the expected resolution, resulting from the scaling described above, as a function of proton energy for various areal densities of high explosives as well as the same set of curves for various areal densities of uranium. For thin objects radiographed with 20 GeV protons the expected resolution (without detector blur) is 2 microns in a 100 mm field of view. For very thick objects (200g/cm2 of uranium) this same system would provide 350 micron resolution. (C.L. Morris)

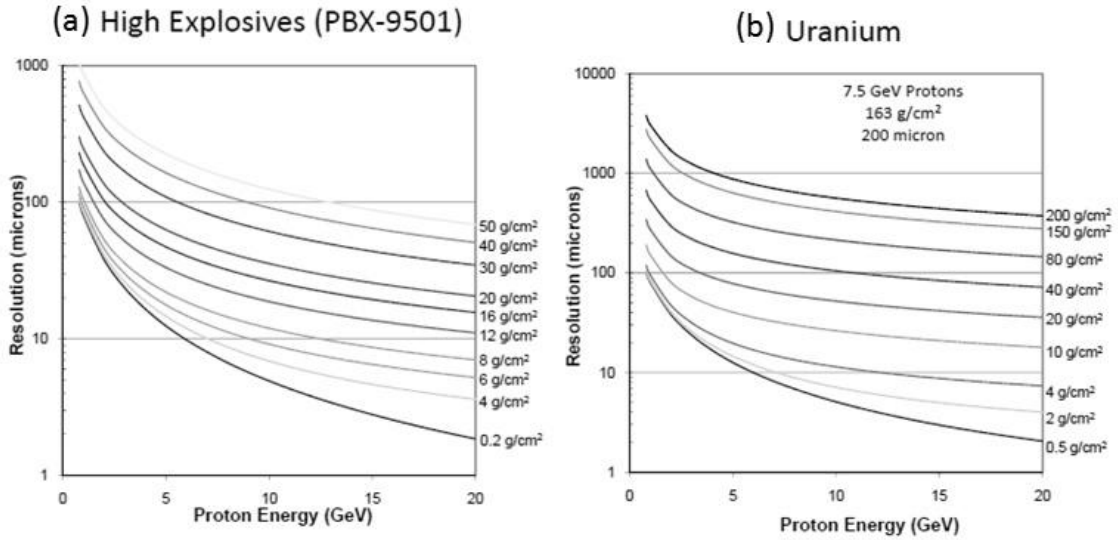

Figure 12: Expected radiographic resolution (without detector blur) in various thicknesses of HE and uranium as function of proton energy from scaling of measurements at 800 MeV.

3.5 Magnification

We have found that magnifying lenses reduce the chromatic length and also reduce the contribution from the detector blur resulting in improved resolution. Using conventional quadrupoles with ~1T pole tip field, this improved resolution comes at the cost of field of view. Figure 13 shows the measured "bare resolution" for 800MeV proton radiography and the resulting field of view as a function of magnification. Magnifying lens systems at 20 GeV could possibly improve the ultimate resolution of the radiography system with a corresponding loss of field of view. High energy magnification has not been studied completely. The ultimate resolution achievable at 20 GeV could be studied with models and measured at the 20 GeV proton radiography facility at the AGS.

Based on our experience, it is reasonable to expect that a X5 magnifier at 20 GeV can be designed to improve the chromatic resolution shown in figure 12 by a factor 5. The resulting expected resolution is shown in figure 14. Resolution at this level would not be achievable at commissioning of a new 20 GeV radiography facility, as there will undoubtedly be new contributions to blur as we move to these very high resolution radiography systems. However, there is no fundamental limit prohibiting sub-micron radiographic capabilities. An ongoing research and development effort in

detector and radiography improvements could lead to future systems with sub-micron resolution on static and dynamic systems. At this level of resolution, however, one has to evaluate the impact of motion blur for dynamic experiments.

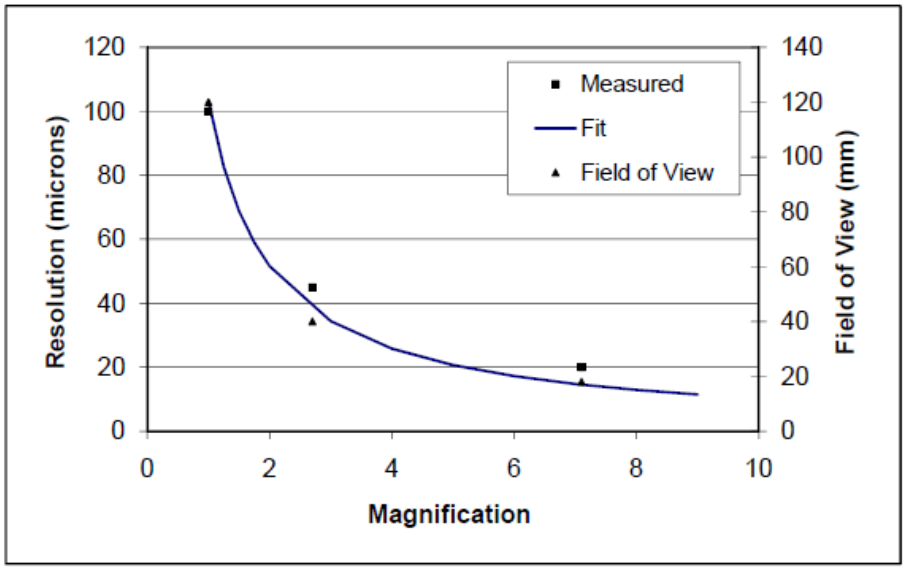

Figure 13: Measured resolution of the magnetic imaging system as a function of magnification with 800MeV proton radiography. The fit to the measured resolution implies that the resolution is proportional to the inverse of the magnification factor.

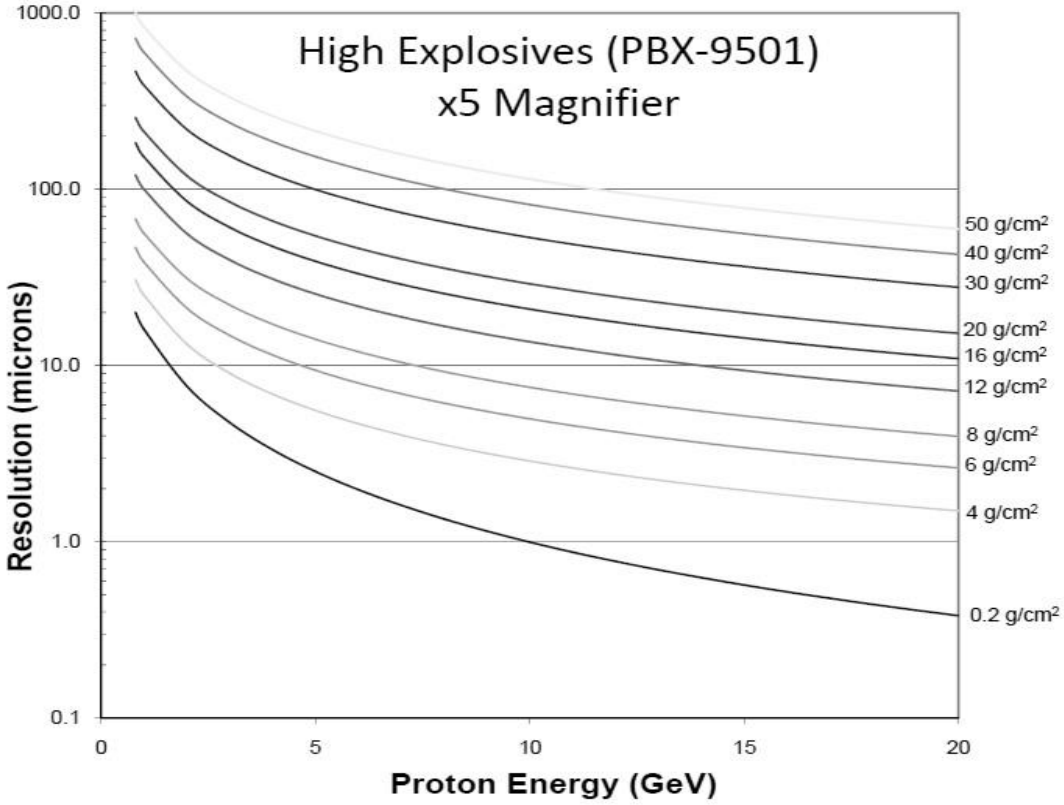

Figure 14: Resolution scaling with proton energy and a magnification of 5. For thin objects, and proton energies greater than 10GeV, it is possible to achieve sub-micron resolution.

4 CONCLUISION

Since its introduction by LANL scientists more than a decade ago, between forty to fifty dynamic experiments are fielded at the pRad facility in Los Alamos every year. Based on the Los Alamos concept, proton radiographic facilities at the Terrawatt Accelerator Institute of Theoretical and Experimental Physics (TWAC-ITEP) in Moscow, Russia and at the Institute of High Energy Physics (IHEP) in Protvino, Russia have been developed. They are routinely used to study the physics of shock-loaded material. Proton radiography has many advantages over x-ray flash radiography including more highly effective doses, low background and ease of extraction of quantitative results(C.L. Morris). The multi-frame capability has provided experimenters a new window into the time evolution of energetic processes. The data on explosives and other energetically driven materials have become important in the validation or modification of existing simulation codes. The suitability of proton tomography of high-Z objects such as nuclear fuel rods has been demonstrated. We have shown that imaging resolution can be improved by using higher energy protons, and, with magnification techniques submicron resolution is achievable. With such resolution the applications of proton radiography can extend to the study of materials at the micron scale. However, for such resolution improvements to be of practical use, parallel developments in detector and camera technology may be required.

REFERENCES

A.J. Clarke, J.C. Cooley, F.E. Merrill, C. Morris, B.J. Hollander, F.G. Mariam, C. Munson, Proton Radiography Team, B.M. Patterson, T.J. Tucker, R.D. Field, D.A. Korzekwa, D.L. Hammon, K.D. Clarke, J. C. Foley, R.M. Aikin, D.J. Thoma, P.S. Dunn, D.F. Tete. *Proton Radiography During Alloy Melting and Solidification Experiments*. Los Alamos: LANL, LA-UR-11-06179, 2011.

C. L. Morris, M. Bourke, D. D. Byler, C. F. Chen, G. Hogan , J. F. Hunter, K. Kwiatkowski, F. G. Mariam, K.J. McClellan, F. Merrill, D.J. Morley, and A. Saunders. *Qualitative Comparison of Bremsstrahlung X-rays and 800 MeV Protons for Tomography of Urania Fuel Pellts*. Los Alamos: LANL, LA-UR-12-23590, 2012.

C. Thomas Motterhead, John D. Zumbro. "Magnetic Optics for Proton radiography." *IEEE* (1998): 1397-1399.

C.L. Morris, N.S.P. King, K. Kwiatkowski, F.G. Mariam, F.E. Merrill, A. Saunders. *Charged particle radiography*. Los Alamos: LANL, LA-UR 12-01545, 2012.

Eric N Ferm, Fesseha Mariam. *Proton radiography Observations of the Failure of a Detonation Wave to Propagate to the End of a Conical Explosive Charge*. Los Alamos: Los Alamos National Laboratory, LA-UR-05-7364, 2005.

F.E. Merrill, E. Campos, C. Espinoza, G. Hogan, B. Hollander, J. Lopez. F.G. Mariam, D. Morley, C.L. Morris, A. Saunders, C. Schwartz, and T.N. Thompson. "Magnifying lens for 800 MeV proton radiography." *Review of Scintific Instruments 82, 103709* (2011): 103709-1 to 103709-6.

Koehler, A.M. "Proton Radiography." *Sceince 160* (1968): 303.

Kris Kwiatokowski, Paul Nedrow, Vincent Douence, Fesseha Mariam, Frank Merrill, Christopher Morris, Andy Saunders, Gary Hogan, Yibin Bai, Atul Joshi. "Ultra-high speed burst-mode imager for multi-frame radiography." *Proc. of the 29th International Congress on High-Speed Imaging and PHotonics, A08 (1020)*. 2010.

MOTTERSHEAD, C. T., BARLOW, D. B., BLIND, B., HOGAN, G. E., JASON, A. J., MERRILL, F. E., MORLEY, K. B., MORRIS, C., SAUNDERS, A. & VALDIVIEZ, R. "Design and operation of a proton microscope for radiography at 800 MEV." *Particle Accelerators*. Portland, Oregon, 2003. Submitted to: 2003 Particle Acc.

P.A. Rigg, C.L. Schwartz, R.S. Hixon, G.E. Hogan, K.K. Kwiatkowski, F.G. Mariam, M. Marr-Lyon, F.E. Merrill, C.L. Morris, P. Rightly, A. Saunders, and D. Tupa. "Proton radiography and accurate density measurements; A window into shock wave processes." *Physical Review B, 77* (2008): 220101-1 to 220101-4.

W.T. Buttler, D.M. Oro, D.L. Preston, K.O. Mikaelian, F.J. Cherne, R.S. Hixon, F.G. Mariam, J.B. Stone, G. Terrones, and D. Tupa. "Unstable Richtmyer-Meshkov growth of solid and liquid metals in vacuum." *J. Fluid Mech. (2012), vol 703* (2012): 60-84.

W.T. Buttler, et al. *2D Richtmeyer Meshkov Instability Growth in Liquified Tin*. Los Alamos: LANL, LA-UR-06-4998, 2006.